

Long-term optical variability of high-mass X-ray binaries. III. Polarimetry

P. Reig^{1,2}, D. Blinov^{1,2}, and A. Tzouvanou^{2,3}

¹ Institute of Astrophysics, Foundation for Research and Technology-Hellas, 71110, Heraklion, Greece

² Physics Department, University of Crete, 71003, Heraklion, Greece – e-mail: pau@physics.uoc.gr; blinov@physics.uoc.gr

³ Max-Planck-Institut für Astronomie, Königstuhl 17, 69117 Heidelberg, Germany – e-mail: tzouvanou@mpia.de

Received ; accepted

ABSTRACT

Context. Be/X-ray binaries are the most numerous group of high-mass X-ray binaries. Their long-term optical and infrared variability reflects the evolution of the circumstellar disk around the luminous companion. This variability manifests photometrically as an excess of flux that increases with wavelength and spectroscopically as line emission. The disk is also expected to generate linear polarization.

Aims. We present a systematic study of the optical long-term polarimetric variability of Be/X-ray binaries on data collected over 10 years. Our aim is to characterize the polarimetric properties of these systems and to probe the structure of their circumstellar disks.

Methods. We have been monitoring Be/X-ray binaries visible from the Northern hemisphere with the RoboPol polarimeter. We performed a careful analysis of the interstellar polarization in the direction of the sources to estimate their intrinsic polarization. Stokes parameters for linear polarization were computed by means of aperture photometry and corrected for instrumental polarization.

Results. Optical polarimetric variability is a common trait in Be/X-ray binaries. The variability can be attributed to the Be star's circumstellar disk. Our polarization analysis confirms previous claims based on spectroscopic data that the circumstellar disks in BeXBs are, on average, smaller and denser than Be stars in non-binary systems. Our data also confirms the presence of highly distorted disk prior to giant X-ray outbursts, although this result is still affected by the lack of simultaneous and well-sampled observations during major X-ray outbursts.

Key words. X-rays: binaries – stars: neutron – stars: binaries close – stars: emission line, Be

1. Introduction

Neutron star high-mass X-ray binaries (HMXB) are accretion-powered binary systems where the neutron star orbits an early-type (O or B) companion. The luminosity class of the optical companion subdivides HMXBs into Be/X-ray binaries (BeXB), when the optical star is a dwarf, subgiant or giant OBe star (luminosity class III, IV or V) and supergiant X-ray binaries (SGXBs), when they contain an evolved star of luminosity class I-II. In SGXBs, the optical star emits a substantial stellar wind. A neutron star in a relatively close orbit will capture a significant fraction of this wind, sufficient to power a bright X-ray source. In BeXB, the donor is a Be star, i.e. a rapidly rotating early-type B star with a gaseous equatorial disk (Reig 2011; Rivinius et al. 2013).

The disk is formed when matter is ejected from the stellar photosphere with sufficient angular momentum. Such disk is referred to as a decretion disk. The ultimate mechanism that lifts material into the disk remains an open question, but the most likely candidates are a combination of fast rotation and non-radial pulsations (Rivinius et al. 2013) or magnetic reconnection associated with localized magnetic fields generated by convection (Balona 2003; Balona & Ozuyar 2021). More recently, Martin et al. (2025) have proposed the presence of a boundary layer that connects a geometrically thick disk to a rotationally flattened star. The boundary layer would provide the required torque and prevent the ejected material from falling back onto the star. In turn, the decretion disk exerts a torque on the star that

slows the Be star's rotation rate while still allowing decretion to continue.

The physical properties of the disk, such as density or physical extent, depend on whether the mass-outflow mechanism is active. Disks in Be stars form and dissipate contributing to their long-term optical/IR variability. Because the disk is also the main reservoir of material available for accretion onto the compact object, its evolution is likewise reflected in the X-ray variability of Be/X-ray binaries. The largest-amplitude variations are typically observed on timescales of years, corresponding to the characteristic timescale for disk build-up and dissipation (Jones et al. 2008; Reig et al. 2016; Treiber et al. 2025).

Circumstellar disks in Be stars contribute to both the continuum and discrete (e.g. line) emission and this contribution is observable in photometry, spectroscopy, and polarimetry:

- Disk emission contributes to the overall brightness of the system and affects the photometric magnitudes and colors. The excess continuum radiation is small at short wavelengths (i.e. *B* band) and increases at longer wavelengths (i.e. *H* and *K* bands). The main disk contribution to the *V* band comes from a relatively small area near the star, whereas the emission area increases for longer wavelengths (Carciofi & Bjorkman 2006). As a result, the color indices increase and the emission becomes redder, as the disk develops.
- The most prominent feature in the optical spectra of Be stars is the presence of emission lines, particularly those of the Balmer series. The hydrogen lines are optically thick and are formed in a large part of the disk by recombination. In particular, the $H\alpha$ line stands out as the primary diagnostic of

Send offprint requests to: pau@physics.uoc.gr

the disk state (Quirrenbach et al. 1997; Tycner et al. 2005; Grundstrom & Gies 2006). Large amplitude variations in the strength and profile morphology are associated with structural changes of the circumstellar decretion disk (Reig et al. 2016).

- The continuum polarization is attributed to Thomson scattering of initially unpolarized stellar radiation in the disk (Coyne & Kruszewski 1969; Serkowski 1970; Poeckert et al. 1979). Thomson scattering polarizes the radiation perpendicular to the scattering plane. The amount of the polarization gives information about the number of scatterers (i.e. density). Consequently, changes in the polarization degree and position angle over time trace the evolution of the disk’s physical structure.

We have been monitoring the BeXBs visible from the Northern Hemisphere in the optical band with the 1.3m telescope at Skinakas observatory since 1998, with the aim of investigating the evolution of their decretion disks. The monitoring consists of *BVRI* photometry and medium resolution spectroscopy around the $H\alpha$ line. The results from the photometric study were presented in Reig & Fabregat (2015), while those from the spectroscopic observations were reported in Reig et al. (2016). Since 2013, following the installation of the RoboPol polarimeter, we have also obtained optical polarimetric measurements of the same sources. The present work constitutes the third part of this series and reports the results of the polarimetric observations.

2. Data acquisition and analysis

2.1. Observations

The data were obtained from the Skinakas Observatory (SKO), located on the Ida mountain in central Crete (Greece) at an altitude of 1750 m. The observations were made with the RoboPol polarimeter attached to the 1.3m modified Ritchey-Chrétien telescope, an Andor DW436 CCD with an array of 2048×2048 $13.5 \mu\text{m}$ pixel size (corresponding to $0.435 \text{ arcsec/pixel}$ on sky), hence providing a field of view of 13 square arcmin. The camera was cooled to -70°C ensuring negligible dark current. The default monitoring set-up uses a Johnson-Cousins R-band filter. However, observations at other bandpasses are possible thanks to a five-slot filter wheel.

RoboPol is a four-channel imaging polarimeter that uses two Wollaston prisms and two non-rotating half-wave plates to produce simultaneous measurements of the Stokes Q and U parameters (Ramaprakash et al. 2019). RoboPol splits the incoming light into two light beams one light beam horizontally and the other one vertically (see Fig. 1 in King et al. 2014). Thus, every point in the sky appears four times on the CCD. In each spot the photon counts, measured using aperture photometry, are used to calculate the normalized Stokes parameters $q = Q/I$ and $u = U/I$ of linear polarization, where I is the total intensity of the source. A mask is placed in the telescope focal plane to optimize the instrument sensitivity. The absence of moving parts avoids possible errors caused by variations in sky conditions between measurements. The list of targets is given in Table 1 and the polarization measurements of each individual target are presented as supplementary material (Appendix D) and are archived in the Zenodo repository: <https://doi.org/10.5281/zenodo.18346735>.

2.2. Instrumental polarization

When light passes through the various optical elements that constitute the optical system (telescope plus polarimeter), a low

level polarization is introduced into the observed radiation. This instrumental polarization appears as an additional polarization signal that must be corrected for. We accounted for this effect by measuring zero-polarized standard stars observed over multiple years. The average instrumental polarization in the R band is $0.4 \pm 0.2\%$.

The data must also be corrected to align the rotation of the instrumental $q - u$ plane with respect to the standard reference frame. This was done using highly polarized standards that were monitored along with the unpolarized standard candidates sample. More details on how these two corrections were performed can be found in Blinov et al. (2023).

2.3. Field stars

The light emitted by the star travels through the interstellar medium (ISM) before is detected by the observer. ISM introduces extra polarization that results from the non-sphericity of the dust grains that become oriented in a preferred direction due to the galactic magnetic field (Lazarian et al. 2015; Tram & Hoang 2022). To correct for this extra polarization, we observed a number of field stars in the field of view of each target. The field stars were selected for its proximity in absolute distance with the targets. The interstellar component is removed by vector subtraction. The polarization measurements of the field stars are presented as supplementary material (Appendix E) and are archived in the Zenodo repository: <https://doi.org/10.5281/zenodo.18346735>.

2.4. Data analysis

The data were processed using the standard RoboPol pipeline, which is described by King et al. (2014), with modifications presented by Blinov et al. (2021). The pipeline reads the raw images from the telescope and computes the Stokes parameters of the stars in the field of view by means of aperture photometry. Basically, it performs five tasks: *i*) source identification, *ii*) aperture photometry, *iii*) calibration, *iv*) polarimetry, and *v*) relative photometry

The polarization degree (p) is defined as a function of the normalized Stokes parameters as

$$p = \sqrt{q^2 + u^2} \quad (1)$$

and the corresponding uncertainty

$$\sigma_p = \sqrt{\frac{q^2 \sigma_q^2 + u^2 \sigma_u^2}{q^2 + u^2}} \quad (2)$$

where σ_q and σ_u are the uncertainties of the individual observations and include the contribution from the instrumental error uncertainty

$$\sigma_q = \sqrt{(\sigma_q^{\text{obs}})^2 + (\sigma_q^{\text{inst}})^2} \quad (3)$$

and similarly for u . Unlike u and q which are unbiased quantities and follow a normal distribution, the polarization degree is biased toward higher values at low signal-to-noise ratios and follows a Rician distribution. There are a variety of methods suggested for correction of the bias (Simmons & Stewart 1985; Vaillancourt 2006; Plaszczyński et al. 2014). In this work, we

Table 1: Target list and relevant information.

Source name	Spectral type	V-band (mag)	P _{spin} (s)	P _{orb} (days)	<i>e</i>	Distance (kpc) Gaia DR3	References
4U 0115+63	B0.2Ve	15.4	3.6	24.3	0.34	5.7 ^{+0.5} _{-0.4}	[1a], [1b]
IGR J01363+6610	B1IV-Ve	13.3	–	–	–	5.6 ± 0.4	[2a], [2b]
RX J0146.9+6121	B1Ve	11.3	1400	303?	–	2.75 ± 0.15	[3a], [3b]
IGR J01583+6713	B2IVe	14.4	–	–	–	5.6 ^{+0.6} _{-0.4}	[4a], [4b]
RX J0240.4+6112	B0Ve	10.8	–	26.5	0.54	2.50 ± 0.07	[5a], [5b]
Swift J0243.6+6124	O9.5Ve	12.8	9.9	27.6	0.10	5.2 ^{+0.3} _{-0.2}	[6a], [6b]
V 0332+53	O8–9Ve	15.4	4.4	33.8	0.37	5.9 ± 0.4	[7a], [7b]
RX J0440.9+4431	B0.2Ve	10.7	202.5	150	–	2.44 ^{+0.08} _{-0.09}	[8a], [8b]
1A 0535+262	O9.7IIIe	9.2	105	111	0.47	1.77 ± 0.06	[9a], [9b]
IGR J06074+2205	B0.5Ve	12.2	373.2	80?	–	6.0 ^{+0.9} _{-0.6}	[10a], [10b]
MXB 0656–072	O9.5Ve	12.3	160.4	101.2	0.4?	5.7 ± 0.5	[11a], [11b]
XTE J1946+274	B0-1V-IVe	16.6	15.8	172	0.25	12.1 ^{+2.6} _{-2.2}	[12a], [12b]
KS 1947+300	B0Ve	14.5	18.7	40.4	0.03	14 ⁺³ ₋₂	[13a], [13b]
EXO 2030+375	B0Ve	19.5	42	46.02	0.41	2.4 ^{+0.5} _{-0.4}	[14a], [14b]
GRO J2058+42	O9.5-B0IV-Ve	14.9	192	110	–	8.9 ^{+0.7} _{-0.8}	[15a], [15b]
SAX J2103.5+4545	B0Ve	13.9	358	12.7	0.40	6.2 ^{+0.8} _{-0.5}	[16a], [16b]
IGR J21343+4738	B1IVe	14.1	320	–	–	8.5 ^{+1.1} _{-0.8}	[17]
Cep X–4	B1-2Ve	14.3	66.3	–	–	7.2 ^{+0.68} _{-0.6}	[18]
4U 2206+54	O9.5Ve	9.8	5550	19.2	0.15	3.2 ^{+0.2} _{-0.1}	[19a], [19b]
SAX J2239.3+6116	B0Ve	14.4	1247	263	–	7.3 ^{+0.7} _{-0.5}	[20a], [20b]
IGR J22534+6243	B1Ve	15.3	46.67	–	–	8.9 ^{+1.4} _{-0.9}	[21]

Notes. Distance from Bailer-Jones et al. (2021)

References. [1a] Negueruela & Okazaki (2001); [1b] Raichur & Paul (2010); [2a] Reig et al. (2005b); [2b] Tomsick et al. (2011); [3a] Reig et al. (1997b); [3b] Sarty et al. (2009); [4a] Wang (2010); [4b] Kaur et al. (2008); [5a] Aragona et al. (2009); [5b] Zamanov et al. (2013); [6a] Wilson-Hodge et al. (2018); [6b] (Reig et al. 2020); [7a] Negueruela et al. (1999); [7b] Doroshenko et al. (2016); [8a] Reig et al. (2005a); [8b] Ferrigno et al. (2013); [9a] Haigh et al. (2004); [9b] Grundstrom et al. (2007); [10a] Reig et al. (2010); [10b] Chhotaray et al. (2024); [11a] Yan et al. (2012); [11b] Nespoli et al. (2012); [12a] Verrecchia et al. (2002); [12b] Marcu-Cheatham et al. (2015); [13a] Galloway et al. (2004); [13b] Liu et al. (2025); [14a] Parmar et al. (1989); [14b] Wilson et al. (2008); [15a] Wilson et al. (1998); [15b] Kızıloğlu et al. (2007); [16a] Baykal et al. (2000); [16b] Reig et al. (2004); [17] Reig & Zezas (2014); [18] Bonnet-Bidaud & Mouchet (1998); [19a] Corbet et al. (2007); [19b] Blay et al. (2006); [20a] in't Zand et al. (2001); [20b] Reig et al. (2017); [21] Esposito et al. (2013)

will use the non debiased values of the polarization degree, unless stated otherwise.

The electric vector polarization angle (EVPA) is defined as

$$EVPA = \frac{1}{2} \arctan\left(\frac{u}{q}\right) \quad (4)$$

Because EVPA does not follow a Gaussian distribution, the uncertainty σ_θ was computed numerically, by solving the following integral

$$\int_{-1\sigma_\theta}^{+1\sigma_\theta} G(\theta; p_0) d\theta = 68.27\% \quad (5)$$

where $G(\theta; \theta_0; p_0)$ is the probability density followed by EPVA (Naghizadeh-Khouei & Clarke 1993)

$$G(\theta; \theta_0; p_0) = \frac{e^{-\frac{\eta_0^2}{2}}}{\sqrt{\pi}} \left\{ \frac{1}{\sqrt{\pi}} + \eta_0 e^{\eta_0^2} [1 + \operatorname{erf}(\eta_0)] \right\} \quad (6)$$

where $\eta_0 = P_0 2 \cos 2(\theta - \theta_0)$ and erf is the Gaussian error function. We refer the reader to Blinov et al. (2023) for further details.

3. Results

In this section we present the results of our polarimetric analysis of the targets (Table 1). Our aim is to investigate if BeXBs are intrinsically polarized and study the connection between the long-term polarimetric variability and the X-ray activity.

To determine whether the source is intrinsically polarized, the ISM polarization must be estimated and subtracted from the observed polarization. There are various ways to assess whether the measured polarization can attributed entirely to the ISM or whether some fraction is intrinsic to the source. These include: *i*) multi-color polarimetry; *ii*) variability analysis; *iii*) empirical relationships between extinction and polarization degree in the Galaxy; *iv*) measurements of the polarization of field stars around the X-ray source.

- The wavelength dependence of interstellar polarization is different from that of a Be star. ISM polarization obeys an empirical relation given by Serkowski et al. (1975)

$$P(\lambda)/P_{\max} = \exp[-k \ln^2(\lambda_{\max}/\lambda)] \quad (7)$$

k determines the width or sharpness of the curve. λ_{\max} is the wavelength at which the polarization is maximum and is directly related to the size of the dust grains (Coyne et al. 1974; Serkowski et al. 1975) and to the total to selective extinction $R = A_V/E(B - V)$ (Whittet & van Breda 1978). The mean

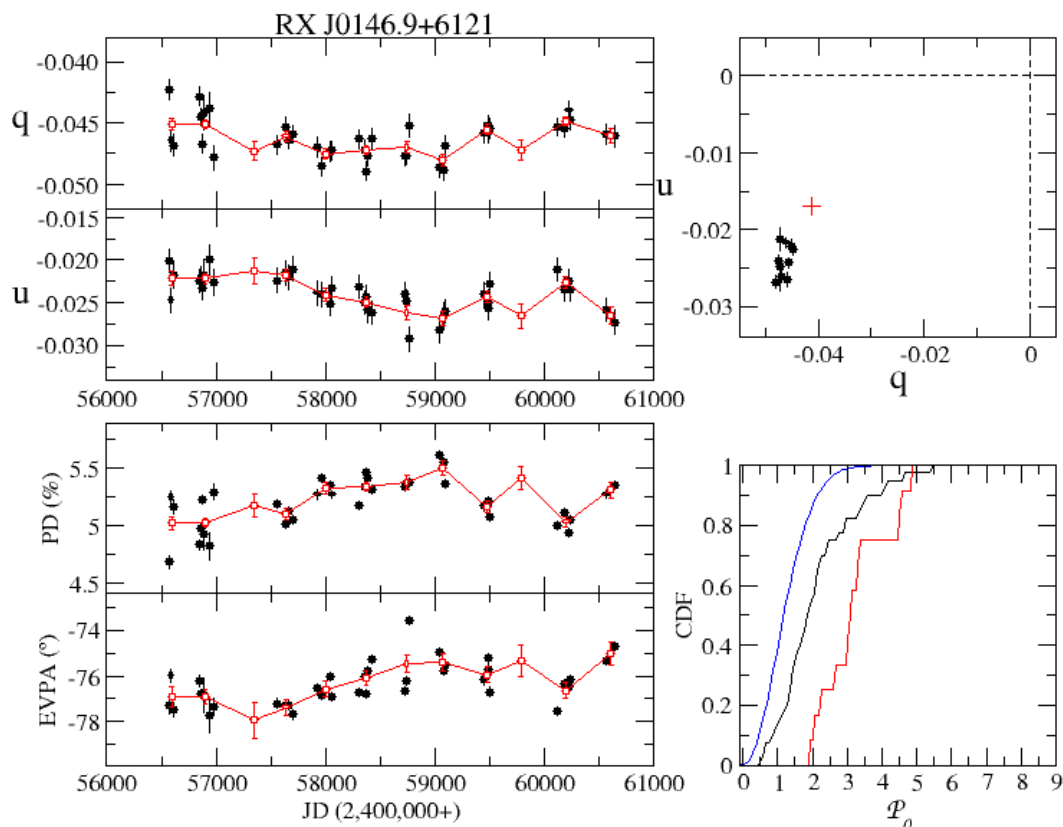


Fig. 1: *Left*: Evolution of the Stokes parameters, polarization degree and angle; *Top-right*: $q - u$ plane. Weighted mean of the source observations (black circles) calculated yearly and of the field stars (red cross); *Bottom-right*: EDF of measured polarization using all data points (black line) or the weighted averaged points (red line) compared with expected CDF of polarization measurements (blue line). See Sect. 3.2 for the meaning of these terms. The data shown correspond to the BeXBs RX J0146.9+6121.

value of $R = 3.05$ corresponds to $\lambda_{\max} = 0.545 \mu\text{m}$ (Whittem & van Breda 1978). A deviation of the Serkowski’s law would indicate a certain amount of intrinsic polarization, although sometimes it can be caused by multiple dust clouds with different properties along the line of sight (Mandarakas et al. 2025). On the other hand, the polarization degree of unreddened Be stars peaks in the blue ($\lambda \approx 0.45 \mu\text{m}$) and decreases with wavelength in the range 0.45-0.80 μm (Poeckert et al. 1979; McDavid 2001; Halonen et al. 2013; Hauboiss et al. 2014).

- Because ISM polarization is expected to remain constant for a given direction, if the polarization degree of a source is variable, then we can conclude that a fraction of it is intrinsic to the source. However, quantifying the actual amount of intrinsic polarization simply through a variability analysis will not be possible unless the nature of the system is such that it allows to define a zero-level intrinsic polarization. Be stars provide such a method. As mentioned above, polarization in Be stars is due to electron scattering in the circumstellar disk. If the disk is absent, then all the contribution to the polarization parameters should come from the ISM. We will discuss disk-loss events in Sect. 4.1.1.
- As the accumulated mass of dust along any line of sight grows with distance, it is expected that the degree of polarization associated with any star will also depend on its distance, or equivalently with extinction. The relationship between polarization and extinction has been studied by a num-

ber of authors (Hiltner 1956; Serkowski et al. 1975; Jones 1989; Reiz & Franco 1998; Fosalba et al. 2002; Ignace et al. 2025). These studies confirm that the ISM polarization fraction increases as the extinction (or distance) increases, albeit with a large scatter. However, these studies are limited to relatively nearby stars with $E(B - V) \lesssim 1$ mag. The alignment and uniformity of the magnetic field is expected to disappear as the line of sight crosses more and more interstellar dust clouds. The resulting polarization of the most distant objects becomes a function of the cloud parameters (orientation and strength of their magnetic field). Thus, the more distant objects are expected to suffer from depolarization. For example, Fosalba et al. (2002) found that the polarization degree as a function of distance shows a maximum for stars at 2 – 4 kpc and then decreases slightly for more distant objects up to 6 kpc. Similarly, using ~ 28000 stars from the catalog of Panopoulou et al. (2025), Ignace et al. (2025) reported that the median polarization fraction increases up to ~ 1 kpc and then flattens out for larger distances.

- The most reliable method for estimating the ISM polarization is to observe a sample of field stars located at distances similar to that of the source. The measured Stokes u and q of the field stars are then subtracted from the measured polarization of our targets.

In the following sections, we address each one of these methods. We only show the results for a selected number of targets,

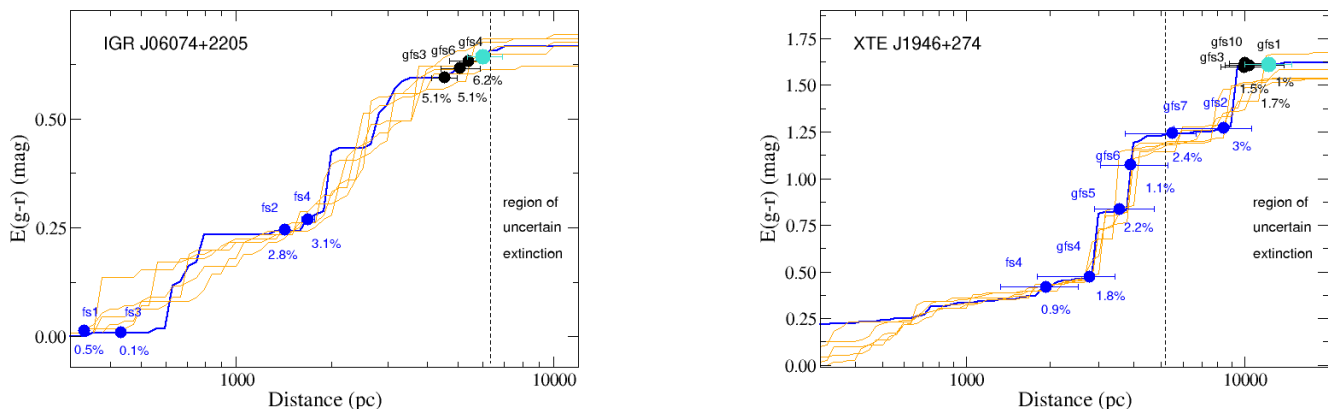


Fig. 2: Two representative examples of the extinction as a function of distance (data from Green et al. 2019). The data points simply mark the assumed location of the stars on the extinction curve, based on their distance but they do not imply any extinction value. Distances are from Bailer-Jones et al. (2021). The turquoise circle represents the BeXB, the black circles are the field stars used for the ISM correction, and the blue circles correspond to other field stars. We also indicate the PD of the field stars. The vertical dashed line marks the region of uncertain extinction.

chosen as representative cases. The results for all the sources are presented in the Appendices.

3.1. Wavelength dependence

Our polarimetric monitoring of the Galactic BeXBs visible from the northern hemisphere was conducted in the R band. However, we also observed several sources in the B , V , and I bands. This multi-color photometry enables, in principle, an investigation of the wavelength dependence of the polarization. In practice, however, due to the scarcity of the data (only four data points) and limited wavelength range, the analysis did not yield conclusive results. Therefore, we did not pursue this method.

3.2. Measuring variability: variability diagram

In this section, we study the long-term polarimetric variability. Since the ISM polarization is expected to remain constant for a given direction and distance in the sky and in order to avoid introducing extra uncertainty inherent to the field stars, the analysis was performed on the data after correcting for instrumental polarization only, without removing the contribution from the ISM.

To study the variability, we follow the methodology explained in Blinov et al. (2023), which in turn, is based on an statistical test using the cumulative distribution function (CDF) of the polarization data (Clarke & Naghizadeh-Khouei 1994; Bastien et al. 2007). The method basically compares the theoretical and empirical cumulative distribution functions (EDF) using a two-sided Kolmogorov-Smirnov (KS) test. If the p -value of the KS test exceeds a given threshold (e.g., $p = 0.0027$ corresponds to 3σ confidence level), we consider the star to be non-variable.

The theoretical CDF for a non-polarized source normalized by its errors $\mathcal{P} = \sqrt{(q/\sigma_q)^2 + (u/\sigma_u)^2}$ is given by

$$CDF(\mathcal{P}) = 1 - e^{-\mathcal{P}^2/2} \quad (8)$$

and the EDF by

$$EDF(\mathcal{P}) = \frac{\text{number of observations} < \mathcal{P}}{\text{total number of observations}} \quad (9)$$

where q and u are the Stokes parameters. For a polarized star, eq. (8) does not apply. One way to circumvent this situation is to subtract the weighted mean \bar{q} and \bar{u} to make the source appear as unpolarized (Clarke & Naghizadeh-Khouei 1994; Blinov et al. 2023)

$$\mathcal{P}_0 = \sqrt{\left(\frac{q - \bar{q}}{\sigma_q}\right)^2 + \left(\frac{u - \bar{u}}{\sigma_u}\right)^2} \quad (10)$$

The plots showing the long-term evolution of the PD and EVPA of all the targets are given in Appendix A. Figure 1 shows the case for the BeXB RXJ0146.9+6121. The left panels in this figure show the evolution of the Stokes parameters u and q and the polarization degree PD and polarization angle $EVPA$. The upper-right panel in Fig. 1 displays the $q - u$ plane. In this panel, the black circles correspond to the weighted mean of the source computed yearly, while the red cross represents the weighted mean of the field stars used later to derive the intrinsic polarization. The bottom-right panel shows the comparison of the theoretical CDF (blue line) and the empirical EDFs for the entire set of observations (i.e. the black circles in the evolution plots, black line) and the seasonal weighted mean (red circles, red line). Instead of assuming a given threshold to assess the variability of the sources, we provide the p -value derived from the KS test¹. Table 2 gives the normal mean and standard deviation of the entire data set for each BeXB. Columns 10 and 11 in this table show the computed p -value of the KS test. We conclude that 18 out of 22 sources are variable at $> 3\sigma$ level on timescales of years.

¹ As a reference, the corresponding p -value for a 2σ confidence level is $p = 0.0455$, for a 3σ is $p = 0.0027$, and for 5σ is $P = 5.733 \times 10^{-7}$. If the computed probability is smaller than p -value, then the source is variable at the given confidence level.

Table 2: Polarization mean and standard deviation. The p -value serves as an indicator of variability. EVPA in the 0° – 180° interval.

Source	PD(%)	σ_{PD} (%)	EVPA ($^\circ$)	σ_{EVPA} ($^\circ$)	q	σ_q	u	σ_u	p-value (all)	p-value (mean)
4U 0115+63	3.66	0.39	110.6	3.1	-0.0275	0.0041	-0.0241	0.0038	3.2×10^{-16}	6.2×10^{-08}
IGR J01363+6610	7.59	0.21	108.4	0.8	-0.0607	0.0019	-0.0456	0.0024	7.1×10^{-01}	1.3×10^{-02}
RX J0146.9+6121	5.20	0.17	103.6	1.1	-0.0462	0.0015	-0.0238	0.0021	1.6×10^{-05}	2.6×10^{-10}
IGR J0158+6713	10.31	0.27	110.4	0.7	-0.0781	0.0025	-0.0673	0.0028	4.2×10^{-01}	9.8×10^{-01}
RX J0240.4+6112	1.22	0.17	138.0	4.1	0.0013	0.0018	-0.0121	0.0017	4.8×10^{-29}	1.1×10^{-14}
Swift J0243.6+6124	3.77	0.18	110.7	1.3	-0.0282	0.0020	-0.0249	0.0014	4.5×10^{-02}	9.6×10^{-05}
V 0332+53	3.57	0.23	115.1	1.8	-0.0229	0.0021	-0.0274	0.0024	2.2×10^{-08}	9.8×10^{-06}
RX J0441.0+4431	1.88	0.21	155.8	3.1	0.0125	0.0018	-0.0141	0.0023	1.0×10^{-12}	7.3×10^{-08}
1A 0535+26	0.79	0.19	0.3	5.1	0.0079	0.0019	0.0001	0.0014	1.1×10^{-10}	3.3×10^{-10}
IGR J06074+2205	6.12	0.38	159.0	2.0	0.0454	0.0017	-0.0410	0.0054	1.3×10^{-10}	2.0×10^{-06}
MXB 0656-072	2.15	0.18	142.6	4.9	0.0056	0.0038	-0.0207	0.0016	6.8×10^{-08}	1.5×10^{-15}
XTE J1946+274	1.77	0.36	31.2	5.4	0.0082	0.0032	0.0157	0.0037	1.1×10^{-17}	1.1×10^{-03}
KS 1947+300	2.62	0.23	23.0	2.5	0.0182	0.0021	0.0189	0.0025	4.8×10^{-13}	8.1×10^{-03}
EXO 2030+375	19.06	1.38	41.2	1.7	0.0250	0.0116	0.1889	0.0139	8.3×10^{-19}	1.5×10^{-10}
GRO J2058+42	4.69	0.33	67.3	2.0	-0.0329	0.0031	0.0334	0.0035	1.6×10^{-11}	8.6×10^{-05}
SAX J2103.5+4545	1.64	0.24	4.9	4.0	0.0161	0.0024	0.0028	0.0023	4.4×10^{-21}	4.6×10^{-06}
IGR J21343+4738	1.61	0.28	41.6	4.1	0.0019	0.0023	0.0160	0.0028	1.8×10^{-08}	6.9×10^{-09}
Cep X-4	2.16	0.20	17.6	3.0	0.0177	0.0018	0.0124	0.0025	2.1×10^{-13}	1.9×10^{-02}
4U 2206+54	4.07	0.20	41.4	1.2	0.0051	0.0017	0.0404	0.0020	5.9×10^{-15}	6.0×10^{-05}
SAX J2239.3+6116	7.38	0.22	62.8	0.9	-0.0429	0.0026	0.0601	0.0020	9.4×10^{-02}	5.4×10^{-02}
IGR J22534+6243	5.23	0.33	67.2	1.8	-0.0366	0.0037	0.0374	0.0030	2.7×10^{-05}	3.9×10^{-02}

3.3. Extinction

The relationship between polarization degree and extinction shows large dispersion. For many years, the theoretical upper limit for optimal alignment efficiency of dust grains with external magnetic fields was $P(\%) = 9E(B - V)$ (Serkowski et al. 1975; Reiz & Franco 1998). However, cases where the observed starlight polarization exceeds the classical upper limit and reach $P_V/E(B - V) = 14\%$ have been reported (Panopoulou et al. 2019; Bartlett & Kobulnicky 2025). Nevertheless, the observed mean correlation between polarization degree and extinction for data averaged in extinction bins is much smaller and deviates slightly from the simple linear correlation, $P(\%) = 3.5E(B - V)^{0.8}$ (Fosalba et al. 2002).

Figure 2 shows the extinction curve for IGR J06074+2205 and XTE J1946+274 as examples of a well-behaved case where the PD increases with distance and a more complex case associated with a larger and more uncertain distance, respectively. We marked the location of field stars and the source according to their distances. The extinction data were taken from the dust maps by Green et al. (2019). These figure provides a simple way to estimate the number of molecular clouds to the source, although it should be noted that the range where the data are reliable is limited to a certain distance range due to the lack of sufficient number of stars with reddening estimates. This range varies from source to source and it is indicated by a vertical dashed line in the figures. The individual extinction curves for each source are presented in Appendix B.

3.4. Field stars

The most common method to account for the ISM polarization is to use field stars. We observed several stars in the vicinity of each target (within ~ 7 arcmin) and at comparable distances. Distances were taken from Gaia DR3 (Bailer-Jones et al. 2021). The polarization measurements of the field stars are given in Appendix E (Supplementary material in Zenodo repository):

<https://doi.org/10.5281/zenodo.18346735>). The weighted means of the Stokes parameters u and q are also shown in the variability plots (Fig. 1). However, this method is not free from uncertainty because the dust distribution (e.g. orientation of the dust grains) and number of intervening molecular clouds along the line of sight may be complex (see the right panel in Fig. 2). In addition, some field stars may exhibit non-zero intrinsic polarization, contrary to the assumption of this method that they are intrinsically unpolarized. It is therefore advisable to employ multiple field stars. Owing to this uncertainty, the results of the observations given in the Appendix correspond to the measured polarization values, without correction for ISM contribution. This approach allows readers to apply their own selection of field stars for ISM subtraction. Appendix C presents the sky charts with the identification of the target and the field stars.

4. Discussion

One of the objectives of this work is to study the evolution of decretion disks in BeXBS through polarization observations. Changes in the polarization angle and polarization degree trace evolutionary changes in the geometry and physical extend of the disk. Electron scattering of unpolarized light generates polarized radiation perpendicular to the scattering plane, which in Be stars coincides with the decretion disk. This is because multiple scattering occurs predominantly in the optically thicker equatorial regions. This biases the orientation of the scattering planes of the multiply scattered photons toward the equatorial plane (Wood et al. 1996). Therefore variability in the polarization angle may reveal the presence of warped disks (Reig & Blinov 2018). Likewise, since the degree of the polarization gives information about the number of scatterers, it can be linked to the density of the disk.

Table 3: Minimum and maximum values of the $H\alpha$ equivalent width: N is the number of measurements. The period analyzed is MJD 56445–60645. Typical errors in $EW(H\alpha)$ are $\lesssim 5\%$.

Source	Min. EW($H\alpha$)	Max. EW($H\alpha$)	N
4U 0115+63	+0.3	-12.1	51
IGR J01363+6610	-47.0	-74.7	33
RX J0146.9+6121	-6.3	-15.4	64
IGR J01583+6713	-59.0	-73.9	23
RX J0240.4+6112	-9.3	-14.5	22
SWIFT J0243.6+6124	-4.6	-11.1	39
V 0332+53	-4.0	-10.5	33
RX J0440.9+4431	-1.6	-12.8	40
1A 0535+262	-8.3	-22.1	22
IGR J06074+2205	+2.6	-11.4	31
MXB 0656-072	-3.2	-19.0	21
XTE J1946+274	-33.6	-44.6	30
KS 1947+300	-7.1	-16.5	40
EXO 2030+375	-	-	-
GRO J2058+42	-0.7	-13.9	60
SAX J2103.5+4545	+3.1	-5.6	53
IGR J21343+4738	+3.0	-8.9	51
Cep X-4	-47.7	-55.0	29
SAX J2239.3+6116	-0.8	-21.9	58
IGR J22534+6243	-2.8	-39.9	20

Table 4: Comparison of the polarization degree during low-optical states including disk-loss events and that obtained from the analysis of field stars.

Source	PD (%) low states	PD (%) field stars	Low state (MJD)
4U 0115+63	3.6 ± 0.1	2.6 ± 0.1	59000-59500
RX J0440.9+4431	2.3 ± 0.1	3.0 ± 0.1	56300-56700
IGR J06074+2205	6.5 ± 0.1	5.5 ± 0.1	57950-58050
MXB 0656-072	2.2 ± 0.1	2.3 ± 0.1	59000-60000
GRO J2058+42	4.4 ± 0.1	2.5 ± 0.1	59700-60500
SAX J2103.5+4545	1.6 ± 0.1	1.6 ± 0.1	59700-59830
IGR J21343+4738	1.3 ± 0.1	1.4 ± 0.1	56500-57300
SAX J2239.3+6116	7.2 ± 0.1	5.8 ± 0.1	57000-57800

4.1. Long-term variability

In Sect. 3.2, we showed that most BeXBs are polarimetric variable sources on timescales of years. Only three systems, SAX J2239.3+6116, IGR J01363+6610 and IGR J0158+6713 display stable long-term polarization ($< 2\sigma$). But even in these cases, the standard deviation computed over the entire data set (Table 2) is significantly larger than the accuracy of the instrument, estimated to be not worse than 0.015% based on measurements of standard stars. These timescales are associated with the viscous time over which the Be star’s disks evolve. Two natural consequences of the long-term variability associated disk evolution are the loss of the disk and the occurrence of X-ray outbursts.

4.1.1. Disk-loss episodes

Circumstellar disks in Be stars, and therefore also in BeXBs, are not permanent features. They form, grow and dissipate on timescales of years. Disk-loss episodes are of paramount importance because they enable the separation of intrinsic polarization from that due to the ISM. In Be stars, linear polarization origi-

nates in the circumstellar disk. Thus, in the absence of the disk, the measured polarization must be entirely interstellar in origin. The $H\alpha$ line is the most reliable indicator of disk dissipation: it changes from emission to a pure absorption profile once the disk has been lost. Consequently, its equivalent width (EW) serves as a robust proxy for disk presence or absence. By convention, EW is negative for emission lines and positive for absorption lines.

Table 3 lists the maximum and minimum values of the $EW(H\alpha)$ for the studied targets during the period 2013-2024 that corresponds to our polarimetric campaigns. The spectroscopic data were obtained with the 1.3m telescope at Skinakas observatory and are part of a long-term monitoring project, as explained in the introduction of this paper². Three BeXBs went through disk-loss episodes: IGR J06074+2205, SAX J2103.5+4545, and IGR J21343+4738, while other five showed evidence for highly debilitated disks: 4U 0115+63, RX J0440.9+4431, MXB 0656-072, GRO J2058+42, and SAX J2239.3+6116. Table 4 compares the PD during low optical states, including disk-loss events with the PD from the analysis of the field stars. In general, the agreement is good, especially for the cases for which the absence of the disk is more evident. For the sources with $EW(H\alpha) > 0$, a small residual disk is expected to be present. For RX J0440.9+4431, the adequacy of the field stars may be questioned, as they are located at longer distance than the target.

4.1.2. Giant X-ray outbursts

It is generally accepted that X-ray outbursts in Be/X-ray binaries originate when mass from the circumstellar disk of the Be star is transferred to the neutron star. However, the exact mechanism of how this happens is still not well understood. The disks in Be/X-ray binaries are often truncated due to the gravitational effects of the neutron star (Reig et al. 1997a; Negueruela & Okazaki 2001; Okazaki & Negueruela 2001; Reig et al. 2016). This truncation raises the question of how substantial amounts of matter can be transferred to the neutron star to trigger the X-ray outbursts. If the disk is truncated, then accretion of large amounts of matter is only feasible if the disk becomes sufficiently asymmetric and dense to exceed the truncation radius. The current theory suggests that giant outbursts occur when the neutron star captures a significant amount of gas from a warped, highly misaligned, and eccentric Be disk (Martin et al. 2011; Okazaki et al. 2013; Martin et al. 2014). Models indicate that such highly distorted disks can result in enhanced mass accretion when the neutron star passes through the warped region. This interaction increases the density and volume of gas available for accretion onto the neutron star, thereby triggering intense X-ray emission.

Observational evidence of warped disks comes from the spectral lines. Low inclination systems give rise to single peak profiles. Double-peak profiles are typical of intermediate inclination systems, while systems seen at high inclination generate shell profiles (Rivinius et al. 2013). Therefore, if all these different profiles are seen in the same source and since the spin axis of the Be star is not expected to change on timescales of days, the appearance of different profiles in the same star can only imply that the disk axis is changing direction. In other words, that there is a warped precessing disk. Changes in the emission line profile in Be and BeXBs have been interpreted as observational evidence for misaligned disks that become warped in their outer

² The spectroscopic observations will be presented in a forthcoming paper. We refer the reader to Reig et al. (2016) for details on the monitoring program.

Table 5: BeXBs that displayed type II outbursts during the period covered by the observations. The flux and luminosity correspond to the peak of the outburst.

X-ray source	Start (MJD)	End (MJD)	Peak (MJD)	BAT flux ⁽²⁾ (ct/cm ² /s)	Flux ^{(2),(3)} (mCrab)	$L_X^{(1),(2),(4)}$ (erg s ⁻¹)
XTE J1946+274	58275	58325	58283	0.035	159	3.56×10^{37}
KS 1947+300	56548	56691	56610	0.071	323	8.48×10^{37}
EXO 2030+375	59406	59547	59465	0.125	568	3.73×10^{37}
GRO J2058+42	58545	58614	58569	0.050	227	2.86×10^{37}
4U 0115+63	57306	57342	57318	0.100	455	2.30×10^{37}
4U 0115+63	57958	57997	57971	0.064	291	1.47×10^{37}
4U 0115+63	60028	60070	60042	0.150	682	3.45×10^{37}
Swift J0243.6+6124	60092	60204	60136	0.260	1182	4.97×10^{37}
V 0332+53	57185	57311	57234	0.220	1000	5.41×10^{37}
RX J0441.0+4431	59935	60080	59977	0.500	2273	2.04×10^{37}
1A 0535+26	59149	59213	59172	2.420	11000	5.54×10^{37}

Notes. ⁽¹⁾ Assumed distances from Table 1; ⁽²⁾ Energy range 15–50 keV; ⁽³⁾ $1 \text{ mCrab} = 0.000220 \text{ ct cm}^{-2} \text{ s}^{-1}$; ⁽⁴⁾ $1 \text{ mCrab} = 1.3 \times 10^{-11} \text{ erg s}^{-1} \text{ cm}^{-2}$

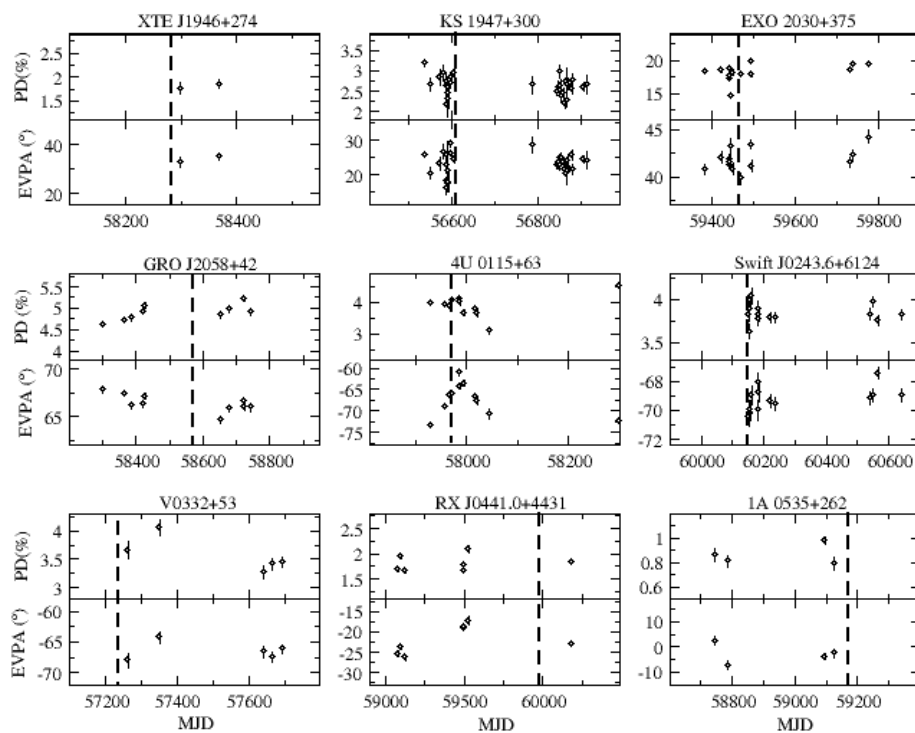


Fig. 3: Polarization degree and angle around the time of a major (type II) X-ray outburst. The vertical dashed lines mark the peak of the X-ray outburst.

parts (Hummel 1998; Negueruela et al. 2001; Reig et al. 2007; Moritani et al. 2011, 2013).

Further evidence for warped disks should come from the polarization angle because light is polarized perpendicular to the scattering plane in Thomson scattering. Therefore, if the orientation of the disk changes, the polarization angle should change as well. Table 5 lists the sources that exhibited a giant (type II) outburst during the period covered by the polarimetric observations. Data were computed from the *Swift*/BAT light curves

by applying the average conversion factors shown in the table footnote. We searched for changes in the polarization parameters during type II outbursts. Figure 3 shows the polarization degree and angle at the time of type II outbursts for the sources that displayed those events during the course of the observations. The vertical dashed lines mark the peak of the X-ray outburst. Unfortunately, the lack of data during many of the outbursts prevents us from providing strong evidence for warped precessing disks. Nevertheless, we found some promising cases.

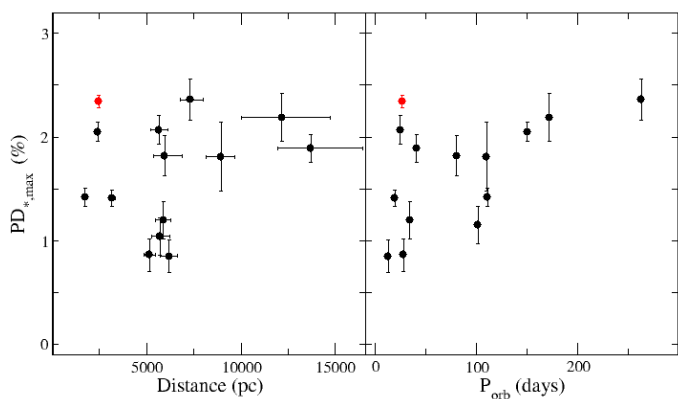


Fig. 4: Maximum intrinsic polarization degree as a function of distance (left) and orbital period (right), excluding the outlier EXO 2030+375. The red point corresponds to the Be/ γ -ray binary RX J0240.4+6112/LS I +61303

In addition to 4U 0115+63, which was already reported in Reig & Blinov (2018), KS 1947+300, EXO 2030+375, and Swift J0243.6+6124 showed changes in the EVPA in coincidence with the X-ray outburst.

The outer parts of the disk are expected to be the most affected by warping effects (Martin & Franchini 2021), while the inner regions, where most of the polarization is produced, would be less affected. Linear polarization signatures arise primarily in the inner parts of the disk, where the density of scatterers is highest (Carciofi 2011; Halonen & Jones 2013b). This fact may explain the relatively small observed EVPA variation ($\lesssim 10^\circ$), which would be associated with the precession angle.

An interesting result that can be extracted from Fig. 3 is that the distorted disk appears to precede the X-ray event. Except for Swift J0243.6+6124, for which no data are available prior to the outburst, the polarization parameters had already begun to vary before the onset of the outburst in the other three cases. In other words, this suggests that the presence of a distorted disk seems to be a prerequisite for triggering an X-ray outburst, consistent with theoretical predictions (Martin et al. 2011; Okazaki et al. 2013; Martin et al. 2014).

4.2. Short-term variability

In addition to long-term variations, Fig. 1 (and Appendix A) also shows significant scatter with variations of 10%–30% of the polarization parameters within timescales of a few weeks to months. This behavior has been seen in isolated Be stars (Vince et al. 1995; Draper et al. 2014). The origin of this generally non-periodic variability is not clear and most likely stems from a diversity of phenomena that lead to changes in the distribution and density of the light scattering material in the disk. Longer-term phenomena (months) associated with this apparent stochastic jumps in the polarization could be a rotating or precessing tilted disk (Marr et al. 2018) or one-armed density waves (Halonen & Jones 2013b; Draper et al. 2014); on much shorter timescales ($\lesssim 1$ day), polarimetric variability may be associated with mass ejection episodes from the Be star into the disk and with stochastic changes in the mass accretion rate (Carciofi et al. 2007; Wisniewski et al. 2010; Carciofi et al. 2025). On intermediate-term timescales (weeks), orbital modulation could also contribute to the scatter (Kravtsov et al. 2020).

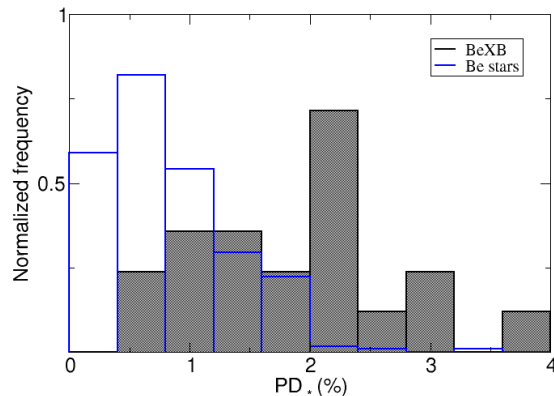


Fig. 5: Normalized histogram (the Y-axis is computed so that the total area under the histogram equals 1) of the maximum intrinsic polarization (corrected for the ISM) of our sample of BeXBs (excluding the outlier EXO 2030+375), compared to the polarization distribution of classical Be stars of similar spectral type (data from Yudin 2001).

4.3. Comparison with Be stars

The circumstellar disks in BeXBs are, on average, smaller and denser than those of Be stars in non-binary systems. Evidence for this result comes from both observations (Reig et al. 1997a, 2000, 2016; Zamanov et al. 2001) and theory (Okazaki et al. 2002; Panoglou et al. 2016; Cyr et al. 2017). This is explained by the interaction between the disk and the neutron star, and more precisely, by disk truncation. The closer the two components of the binary, the stronger the tidal torque exerted by the neutron star on the disk. Systems with short orbital periods ($P_{\text{orb}} \lesssim 50$ d) exhibit faster variability (i.e., rapid, irregular changes) than systems with longer orbital periods (see Fig. 1 in Reig et al. 2016). Clearly, the disk in narrow-orbit systems is exposed to larger torques from the neutron star, preventing it from reaching a stable configuration for a long period of time. Another example is the correlation between the maximum EW($H\alpha$) and the orbital period in BeXBs (Reig et al. 1997a; Reig 2011). Because EW($H\alpha$) provides a measure of the extent of the disk (Tycner et al. 2005; Grundstrom & Gies 2006), the correlation implies that wider-orbit systems are able to develop stable and larger disks.

The question that we investigate here is whether polarization data agree with these results. For this analysis to be meaningful, the intrinsic polarization must be used. The measured polarization was corrected for the contribution of the ISM as indicated in Sect. 3.4. The right panel in Fig. 4 shows the maximum intrinsic polarization degree, P_{*} , as a function of the orbital period, P_{orb} . There is a trend of larger intrinsic PD for wider-orbit systems in BeXBs. The correlation is significant if the outlier EXO 2030+375 and the Be/ γ -ray binary RX J0240.4+6112/LS I +61303 are excluded³: the correlation coefficient and the probability that the null hypothesis (that the two variables are not correlated) is true are $r = 0.66$ and $p\text{-value} = 0.015$, respectively. There are a number of factors that could contribute to the dis-

³ Be/ γ -ray binaries differ from typical BeXBs in the observational as well as emission models for the high-energy radiation. See e.g. Dubus (2013).

persion in this plot. *i*) uncertainty in the ISM polarization estimation, *ii*) the dependence of polarization fraction on inclination angle (Wood et al. 1996; Halonen et al. 2013) and/or *iii*) the fact that polarization takes place closer to the Be star compared to the formation region of the (Carciofi 2011) H α line. In this respect, EW(H α) represents a better proxy for the extent of the disk and the effects of the tidal interaction with the neutron star manifest in a stronger way. The intrinsic polarization fraction and angle strongly depends on the polarization of the field stars. However, the fact that there is no clear trend ($r = 0.26$, p -value=0.34) between the maximum intrinsic polarization and distance (left panel in Fig. 4) implies that, overall, the selection of the field stars was adequate. Nevertheless, a bad representation of the ISM for a few individual systems cannot be ruled out. The case of EXO 2030+375 is unique. It exhibits the highest polarization degree ever measured in either a Be star or a BeXB, well above the typical values observed in these systems (see discussion below). One possible explanation for this apparent extreme behavior is the high and spatially complex extinction toward the source. As shown in Fig. C.1 and Appendix E (Supplementary material in Zenodo repository: <https://doi.org/10.5281/zenodo.18346735>), the polarization degree measured in the vicinity of the X-ray source varies substantially. For instance, clear differences are observed when comparing the spatial locations and polarization degrees of the field stars gfs1 and gfs3, as well as gfs9 and gfs10. In this scenario, the high polarization observed in EXO 2030+375 would not be intrinsic, but rather the result of an inaccurate correction for ISM polarization. An alternative physical explanation for the unusually large PD in EXO 2030+375 was proposed by Reig et al. (2014), who speculated that the high polarization may arise from the alignment of non-spherical ferromagnetic grains in the Be-star disk under the influence of the neutron star's strong magnetic field.

The scatter is larger among the short-period systems ($P_{\text{orb}} \lesssim 50$ d). This is also observed in the H α equivalent width versus orbital period diagram (Reig et al. 2016) and also in the X-ray band (Reig 2007). A simple explanation is that wider orbit systems are able to develop stable disks during longer periods of time. In contrast, the systems with short orbital periods feel the tidal truncation exerted by the neutron star more strongly and more frequently, so that the disk does not easily achieve a stable configuration on shorter timescales.

Yudin (2001) performed a statistical analysis of the intrinsic polarization of 497 isolated Be stars covering the entire spectral range. He found that for the early-type group (B0-B3), which is the relevant group for comparison with BeXBs, the values show larger scatter but on average, Be stars in this spectral range exhibit larger values of polarization. The maximum values of intrinsic polarization for B0-B3 stars are $PD_*(\%) \lesssim 2\%$. In Yudin (2001) sample, only 5 stars exhibited polarization degree above 2% (all in the B0-B2 spectral range). The average intrinsic polarization for different spectral subtypes in Yudin's sample are: $0.84 \pm 0.48\%$ for O-B1.5 and $0.75 \pm 0.48\%$ for B2-B2.5.

We find that about half of our sample of BeXBs display intrinsic maximum polarization degree above 2%. Figure 5 shows the normalized histogram of the maximum measured intrinsic PD in BeXBs compared to classical Be stars of similar spectral type range (data from Yudin 2001). Since the polarization degree reflects the number of scatterers, models predict that as the density increases the polarization level increases because the number of electrons available for Thomson scattering increases (Halonen & Jones 2013a). Therefore, our findings support the idea that disks in BeXBs are denser than in isolated Be stars.

5. Conclusion

We have performed a systematic study of the polarization properties of BeXBs visible from the northern hemisphere to characterize their long-term optical variability and to probe the dynamics and structure of their circumstellar disks. Our findings confirm that BeXBs are intrinsically variable in polarization, with changes in polarization degree and angle directly tracing the evolution of the disk size and geometry. A key result of this work is the confirmation that circumstellar disks in BeXBs are, on average, smaller and significantly denser than those found in isolated Be stars. This is evidenced by the higher intrinsic polarization values observed in our sample, with approximately half of the targets exceeding the typical maximum polarization of isolated Be stars. This finding strongly supports theoretical models of disk truncation, where the gravitational influence of the neutron star tidally truncates and confines the Be star's disk. We also find further evidence linking giant X-ray outbursts to the presence of warped and precessing disks, where changes in the polarization angle, indicating a distorted disk, appear to be a necessary precursor to those high-energy events.

In conclusion, this study highlights the importance of polarimetry as a diagnostic tool, together with spectroscopy and photometry, to investigate the physical mechanisms governing the behavior of these complex binary systems.

6. Data availability

The polarization measurements, including q , u , PD , and $EVPA$ with the corresponding uncertainties, are available on the Zenodo repository <https://doi.org/10.5281/zenodo.18346735>.

Acknowledgements. Skinakas Observatory is a collaborative project of the University of Crete and the Foundation for Research and Technology-Hellas. D.B. acknowledges support from the European Research Council (ERC) under the Horizon ERC Grants 2021 programme under grant agreement No. 101040021. This work made use of NASA's Astrophysics Data System Bibliographic Services and of the SIMBAD database, operated at the CDS, Strasbourg, France. This work has made use of data from the European Space Agency (ESA) mission *Gaia* (<https://www.cosmos.esa.int/gaia>)

References

- Aragona, C., McSwain, M. V., Grundstrom, E. D., et al. 2009, *ApJ*, 698, 514
 Bailer-Jones, C. A. L., Rybizki, J., Fouesneau, M., Demleitner, M., & Andrae, R. 2021, *AJ*, 161, 147
 Balona, L. A. 2003, *Ap&SS*, 284, 121
 Balona, L. A. & Ozuyar, D. 2021, *ApJ*, 921, 5
 Bartlett, J. A. & Kobulnicky, H. A. 2025, *AJ*, 170, 265
 Bastien, P., Vernet, E., Drissen, L., et al. 2007, in *Astronomical Society of the Pacific Conference Series*, Vol. 364, *The Future of Photometric, Spectrophotometric and Polarimetric Standardization*, ed. C. Sterken, 529
 Baykal, A., Stark, M. J., & Swank, J. 2000, *ApJ*, 544, L129
 Blay, P., Negueruela, I., Reig, P., et al. 2006, *A&A*, 446, 1095
 Blinov, D., Kiehlmann, S., Pavlidou, V., et al. 2021, *MNRAS*, 501, 3715
 Blinov, D., Maharana, S., Bouzelou, F., et al. 2023, *A&A*, 677, A144
 Bonnet-Bidaud, J. M. & Mouchet, M. 1998, *A&A*, 332, L9
 Carciofi, A. C. 2011, in *IAU Symposium*, Vol. 272, *IAU Symposium*, ed. C. Neiner, G. Wade, G. Meynet, & G. Peters, 325–336
 Carciofi, A. C. & Bjorkman, J. E. 2006, *ApJ*, 639, 1081
 Carciofi, A. C., Bolzan, G. P. P., Querido, P. R., et al. 2025, *Galaxies*, 13, 77
 Carciofi, A. C., Magalhães, A. M., Leister, N. V., Bjorkman, J. E., & Levenhagen, R. S. 2007, *ApJ*, 671, L49
 Chhotaray, B., Naik, S., Jaisawal, G. K., & Ahuja, G. 2024, *MNRAS*, 534, 2830
 Clarke, D. & Naghizadeh-Khouei, J. 1994, *AJ*, 108, 687
 Corbet, R. H. D., Markwardt, C. B., & Tueller, J. 2007, *ApJ*, 655, 458
 Coyne, G. V., Gehrels, T., & Serkowski, K. 1974, *AJ*, 79, 581
 Coyne, G. V. & Kruszewski, A. 1969, *AJ*, 74, 528
 Cyr, I. H., Jones, C. E., Panoglou, D., Carciofi, A. C., & Okazaki, A. T. 2017, *MNRAS*, 471, 596

- Doroshenko, V., Tsygankov, S., & Santangelo, A. 2016, *A&A*, 589, A72
- Draper, Z. H., Wisniewski, J. P., Bjorkman, K. S., et al. 2014, *ApJ*, 786, 120
- Dubus, G. 2013, *A&A Rev.*, 21, 64
- Esposito, P., Israel, G. L., Sidoli, L., et al. 2013, *MNRAS*, 433, 2028
- Ferrigno, C., Farinelli, R., Bozzo, E., et al. 2013, *A&A*, 553, A103
- Fosalba, P., Lazarian, A., Prunet, S., & Tauber, J. A. 2002, *ApJ*, 564, 762
- Galloway, D. K., Morgan, E. H., & Levine, A. M. 2004, *ApJ*, 613, 1164
- Green, G. M., Schlafly, E., Zucker, C., Speagle, J. S., & Finkbeiner, D. 2019, *ApJ*, 887, 93
- Grundstrom, E. D., Boyajian, T. S., Finch, C., et al. 2007, *ApJ*, 660, 1398
- Grundstrom, E. D. & Gies, D. R. 2006, *ApJ*, 651, L53
- Haigh, N. J., Coe, M. J., & Fabregat, J. 2004, *MNRAS*, 350, 1457
- Halonen, R. J. & Jones, C. E. 2013a, *ApJ*, 765, 17
- Halonen, R. J. & Jones, C. E. 2013b, *ApJS*, 208, 3
- Halonen, R. J., Mackay, F. E., & Jones, C. E. 2013, *ApJS*, 204, 11
- Haubois, X., Mota, B. C., Carciofi, A. C., et al. 2014, *ApJ*, 785, 12
- Hiltner, W. A. 1956, *ApJS*, 2, 389
- Hummel, W. 1998, *A&A*, 330, 243
- Ignace, R., Fullard, A. G., Panopoulou, G. V., et al. 2025, *Ap&SS*, 370, 57
- in't Zand, J. J. M., Swank, J., Corbet, R. H. D., & Markwardt, C. B. 2001, *A&A*, 380, L26
- Jones, C. E., Sigut, T. A. A., & Porter, J. M. 2008, *MNRAS*, 386, 1922
- Jones, T. J. 1989, *ApJ*, 346, 728
- Kaur, R., Paul, B., Kumar, B., & Sagar, R. 2008, *MNRAS*, 386, 2253
- King, O. G., Blinov, D., Ramaprakash, A. N., et al. 2014, *MNRAS*, 442, 1706
- Kızıloğlu, U., Kızıloğlu, N., Baykal, A., Yerli, S. K., & Özbey, M. 2007, *A&A*, 470, 1023
- Kravtsov, V., Berdyugin, A. V., Piirola, V., et al. 2020, *A&A*, 643, A170
- Lazarian, A., Andersson, B.-G., & Hoang, T. 2015, in *Polarimetry of Stars and Planetary Systems*, ed. L. Kolokolova, J. Hough, & A.-C. Levasseur-Regourd, 81
- Liu, W., Reig, P., Yan, J., et al. 2025, *ApJ*, 985, 162
- Mandarakas, N., Tassis, K., & Skalidis, R. 2025, *A&A*, 698, A168
- Marcu-Cheatham, D. M., Pottschmidt, K., Kühnel, M., et al. 2015, *ApJ*, 815, 44
- Marr, K. C., Jones, C. E., & Halonen, R. J. 2018, *ApJ*, 852, 103
- Martin, R. G. & Franchini, A. 2021, *ApJ*, 922, L37
- Martin, R. G., Lubow, S. H., Vallet, D., et al. 2025, *MNRAS*, 539, L31
- Martin, R. G., Nixon, C., Armitage, P. J., Lubow, S. H., & Price, D. J. 2014, *ApJ*, 790, L34
- Martin, R. G., Pringle, J. E., Tout, C. A., & Lubow, S. H. 2011, *MNRAS*, 416, 2827
- McDavid, D. 2001, *ApJ*, 553, 1027
- Moritani, Y., Nogami, D., Okazaki, A. T., et al. 2011, *PASJ*, 63, 25
- Moritani, Y., Nogami, D., Okazaki, A. T., et al. 2013, *PASJ*, 65, 83
- Naghizadeh-Khouei, J. & Clarke, D. 1993, *A&A*, 274, 968
- Negueruela, I. & Okazaki, A. T. 2001, *A&A*, 369, 108
- Negueruela, I., Okazaki, A. T., Fabregat, J., et al. 2001, *A&A*, 369, 117
- Negueruela, I., Roche, P., Fabregat, J., & Coe, M. J. 1999, *MNRAS*, 307, 695
- Nespoli, E., Reig, P., & Zezas, A. 2012, *A&A*, 547, A103
- Okazaki, A. T., Bate, M. R., Ogilvie, G. I., & Pringle, J. E. 2002, *MNRAS*, 337, 967
- Okazaki, A. T., Hayasaki, K., & Moritani, Y. 2013, *PASJ*, 65, 41
- Okazaki, A. T. & Negueruela, I. 2001, *A&A*, 377, 161
- Panoglou, D., Carciofi, A. C., Vieira, R. G., et al. 2016, *MNRAS*, 461, 2616
- Panopoulou, G. V., Hensley, B. S., Skalidis, R., Blinov, D., & Tassis, K. 2019, *A&A*, 624, L8
- Panopoulou, G. V., Markopouloti, L., Bouzelou, F., et al. 2025, *ApJS*, 276, 15
- Parmar, A. N., White, N. E., Stella, L., Izzo, C., & Ferri, P. 1989, *ApJ*, 338, 359
- Plaszczynski, S., Montier, L., Levrier, F., & Tristram, M. 2014, *MNRAS*, 439, 4048
- Poecckert, R., Bastien, P., & Landstreet, J. D. 1979, *AJ*, 84, 812
- Quirrenbach, A., Bjorkman, K. S., Bjorkman, J. E., et al. 1997, *ApJ*, 479, 477
- Raichur, H. & Paul, B. 2010, *MNRAS*, 406, 2663
- Ramaprakash, A. N., Rajarshi, C. V., Das, H. K., et al. 2019, *MNRAS*, 485, 2355
- Reig, P. 2007, *MNRAS*, 377, 867
- Reig, P. 2011, *Ap&SS*, 332, 1
- Reig, P., Blay, P., & Blinov, D. 2017, *A&A*, 598, A16
- Reig, P. & Blinov, D. 2018, *A&A*, 619, A19
- Reig, P., Blinov, D., Papadakis, I., Kylafis, N., & Tassis, K. 2014, *MNRAS*, 445, 4235
- Reig, P. & Fabregat, J. 2015, *A&A*, 574, A33
- Reig, P., Fabregat, J., & Alfonso-Garzón, J. 2020, *A&A*, 640, A35
- Reig, P., Fabregat, J., & Coe, M. J. 1997a, *A&A*, 322, 193
- Reig, P., Fabregat, J., Coe, M. J., et al. 1997b, *A&A*, 322, 183
- Reig, P., Larionov, V., Negueruela, I., Arkharov, A. A., & Kudryavtseva, N. A. 2007, *A&A*, 462, 1081
- Reig, P., Negueruela, I., Coe, M. J., et al. 2000, *MNRAS*, 317, 205
- Reig, P., Negueruela, I., Fabregat, J., et al. 2004, *A&A*, 421, 673
- Reig, P., Negueruela, I., Fabregat, J., Chato, R., & Coe, M. J. 2005a, *A&A*, 440, 1079
- Reig, P., Negueruela, I., Papamastorakis, G., Manousakis, A., & Kougentakis, T. 2005b, *A&A*, 440, 637
- Reig, P., Nersesian, A., Zezas, A., Gkouvelis, L., & Coe, M. J. 2016, *A&A*, 590, A122
- Reig, P. & Zezas, A. 2014, *A&A*, 561, A137
- Reig, P., Zezas, A., & Gkouvelis, L. 2010, *A&A*, 522, A107
- Reiz, A. & Franco, G. A. P. 1998, *A&AS*, 130, 133
- Rivinius, T., Carciofi, A. C., & Martayan, C. 2013, *A&A Rev.*, 21, 69
- Sarty, G. E., Kiss, L. L., Huziak, R., et al. 2009, *MNRAS*, 392, 1242
- Serkowski, K. 1970, *ApJ*, 160, 1083
- Serkowski, K., Mathewson, D. S., & Ford, V. L. 1975, *ApJ*, 196, 261
- Simmons, J. F. L. & Stewart, B. G. 1985, *A&A*, 142, 100
- Tomsick, J. A., Heinke, C., Halpern, J., et al. 2011, *ApJ*, 728, 86
- Tram, L. N. & Hoang, T. 2022, *Frontiers in Astronomy and Space Sciences*, 9, 923927
- Treiber, H., Vasilopoulos, G., Baily, C. D., Haberl, F., & Udalski, A. 2025, *A&A*, 694, A43
- Tycner, C., Lester, J. B., Hajian, A. R., et al. 2005, *ApJ*, 624, 359
- Vaillancourt, J. E. 2006, *PASP*, 118, 1340
- Verrecchia, F., Israel, G. L., Negueruela, I., et al. 2002, *A&A*, 393, 983
- Vince, I., Arsenijević, J., Marković-Kršljanin, S., Jankov, S., & Skuljan, L. 1995, *International Amateur-Professional Photoelectric Photometry Communications*, 59, 32
- Wang, W. 2010, *A&A*, 516, A15
- Whittet, D. C. B. & van Breda, I. G. 1978, *A&A*, 66, 57
- Wilson, C. A., Finger, M. H., & Camero-Arranz, A. 2008, *ApJ*, 678, 1263
- Wilson, C. A., Finger, M. H., Harmon, B. A., Chakrabarty, D., & Strohmayer, T. 1998, *ApJ*, 499, 820
- Wilson-Hodge, C. A., Malacaria, C., Jenke, P. A., et al. 2018, *ApJ*, 863, 9
- Wisniewski, J. P., Draper, Z. H., Bjorkman, K. S., et al. 2010, *ApJ*, 709, 1306
- Wood, K., Bjorkman, J. E., Whitney, B. A., & Code, A. D. 1996, *ApJ*, 461, 828
- Yan, J., Zurita Heras, J. A., Chaty, S., Li, H., & Liu, Q. 2012, *ApJ*, 753, 73
- Yudin, R. V. 2001, *A&A*, 368, 912
- Zamanov, R., Stoyanov, K., Martí, J., et al. 2013, *A&A*, 559, A87
- Zamanov, R. K., Reig, P., Martí, J., et al. 2001, *A&A*, 367, 884

Appendix A: Long-term polarimetric variability of targets

This appendix gives the evolution of the polarization observations of the targets.

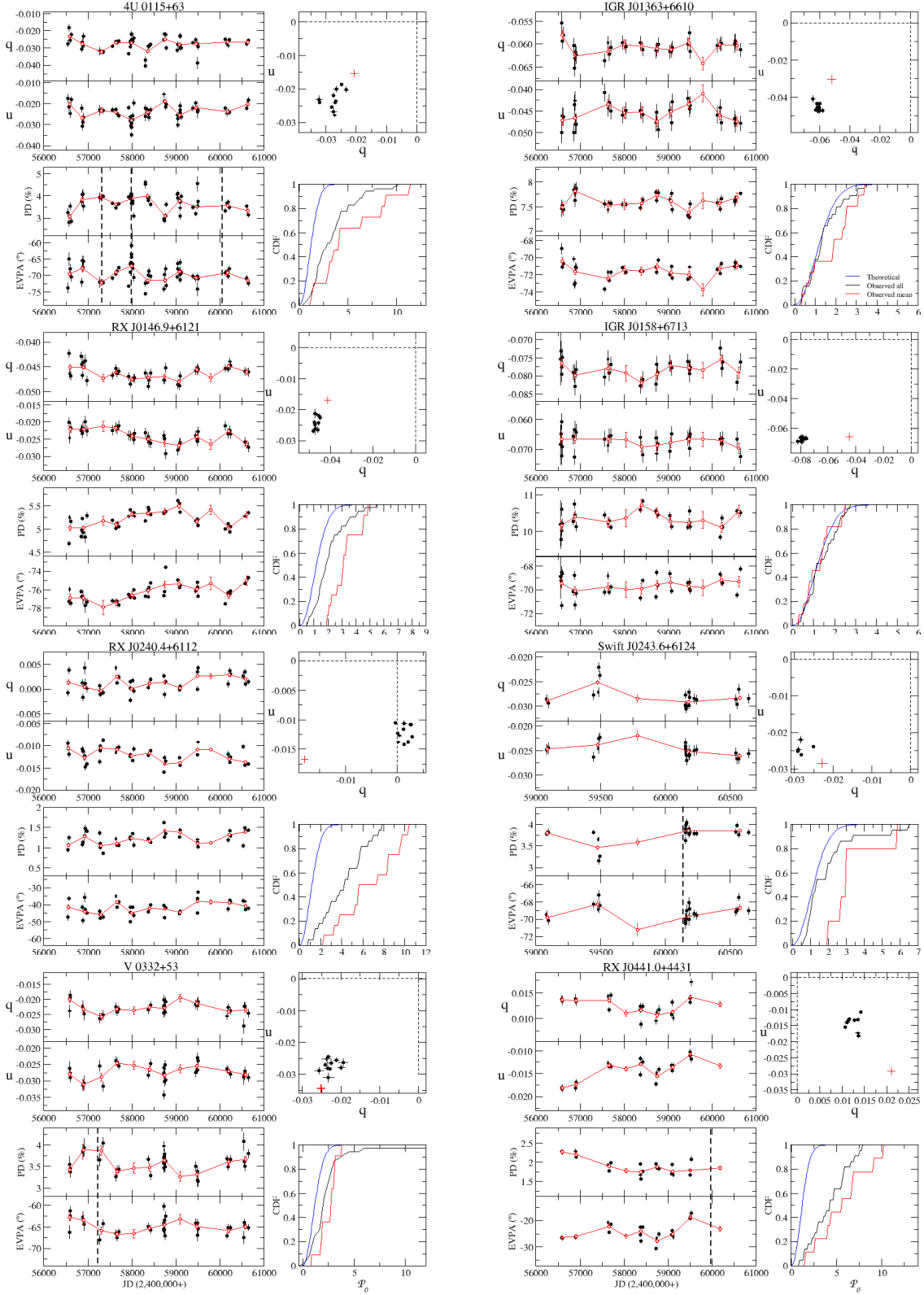


Fig. A.1: *Left panels:* Evolution of the Stokes parameters, polarization degree and angle; *Top-right panel:* $q-u$ plane. Weighted mean of the source observations (black circles) calculated yearly and of the field stars (red cross); *Bottom-right panel:* EDF of measured polarization using all data points (black line) or the weighted averaged points (red line) compared with expected (theoretical) CDF of polarization measurements (blue line).

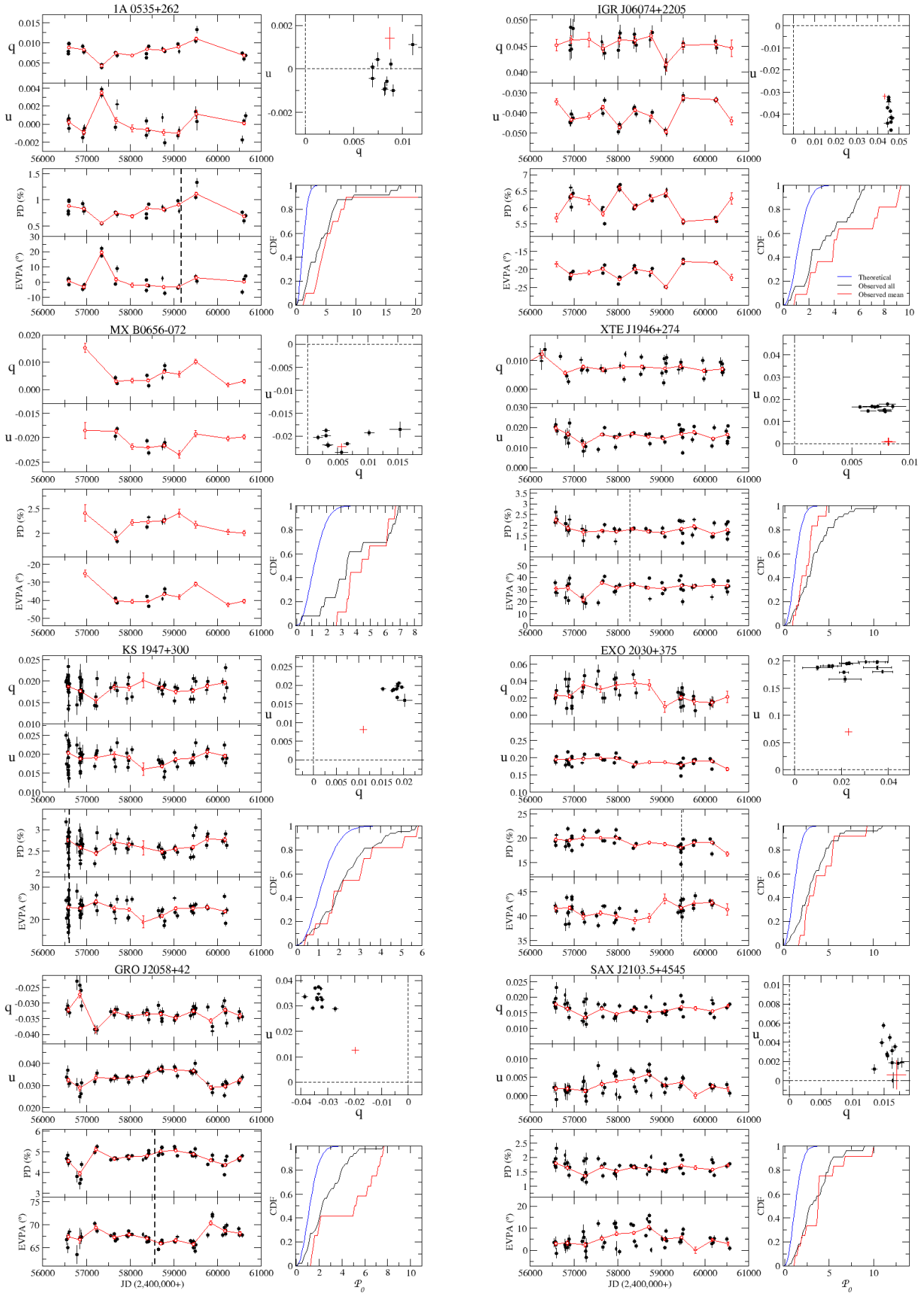


Fig. A.1: Continued.

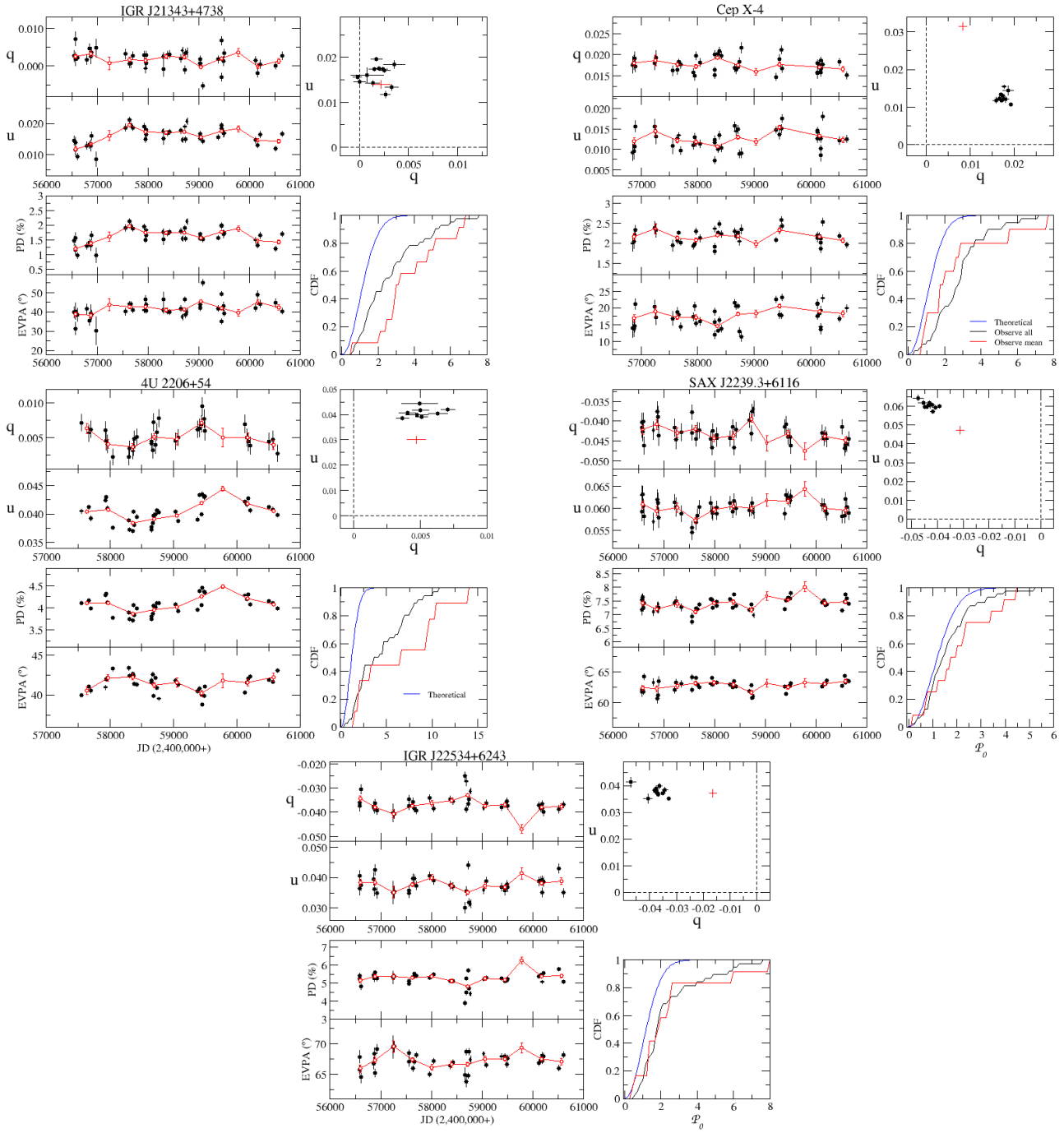


Fig. A.1: Continued.

Appendix B: Extinction curves

This appendix shows the extinction curves for each individual target.

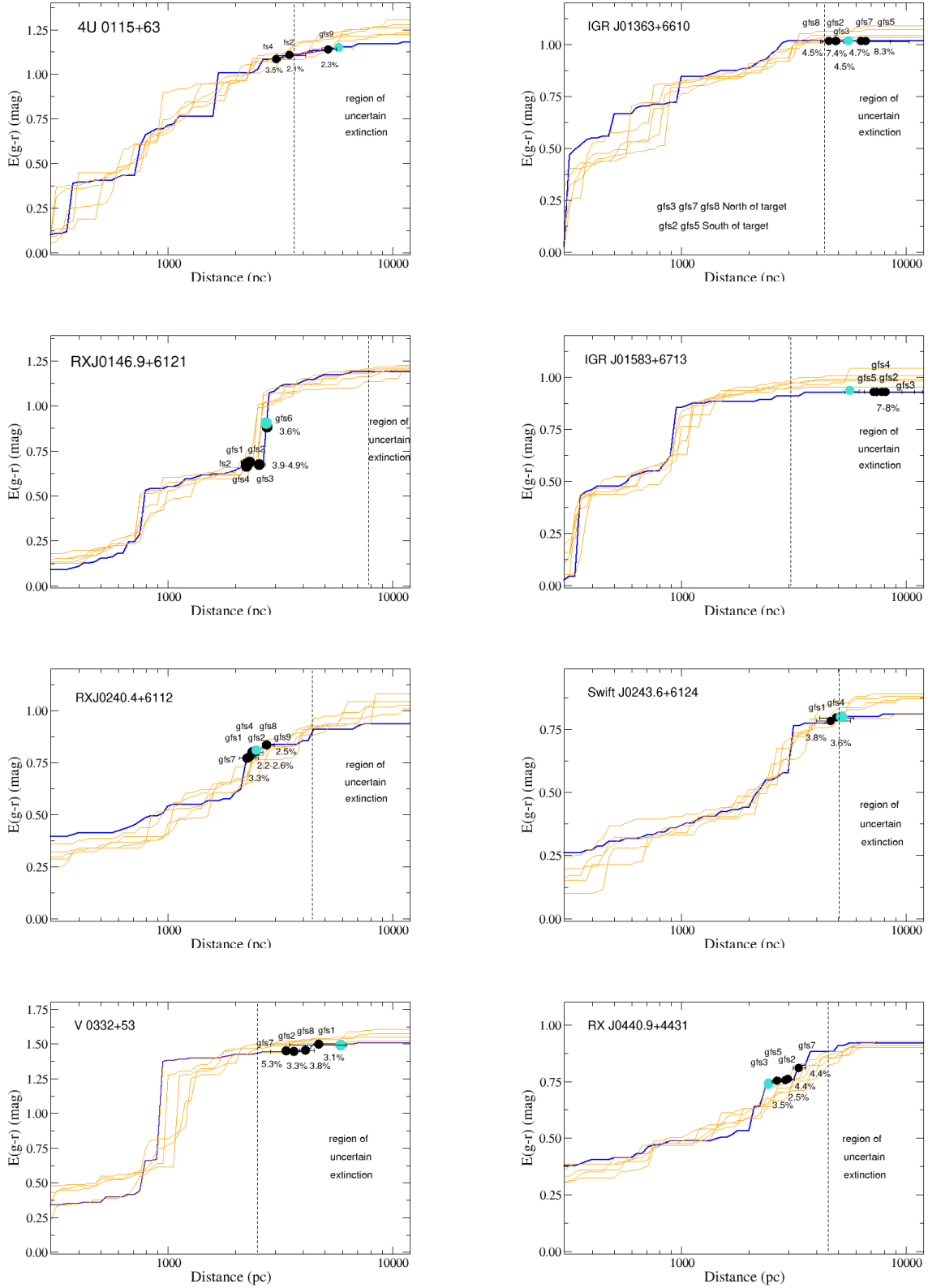


Fig. B.1: Extinction as a function of distance in the direction of the targets. The turquoise circle represents the target, while the black circles correspond to the field stars that were used to correct for ISM polarization.

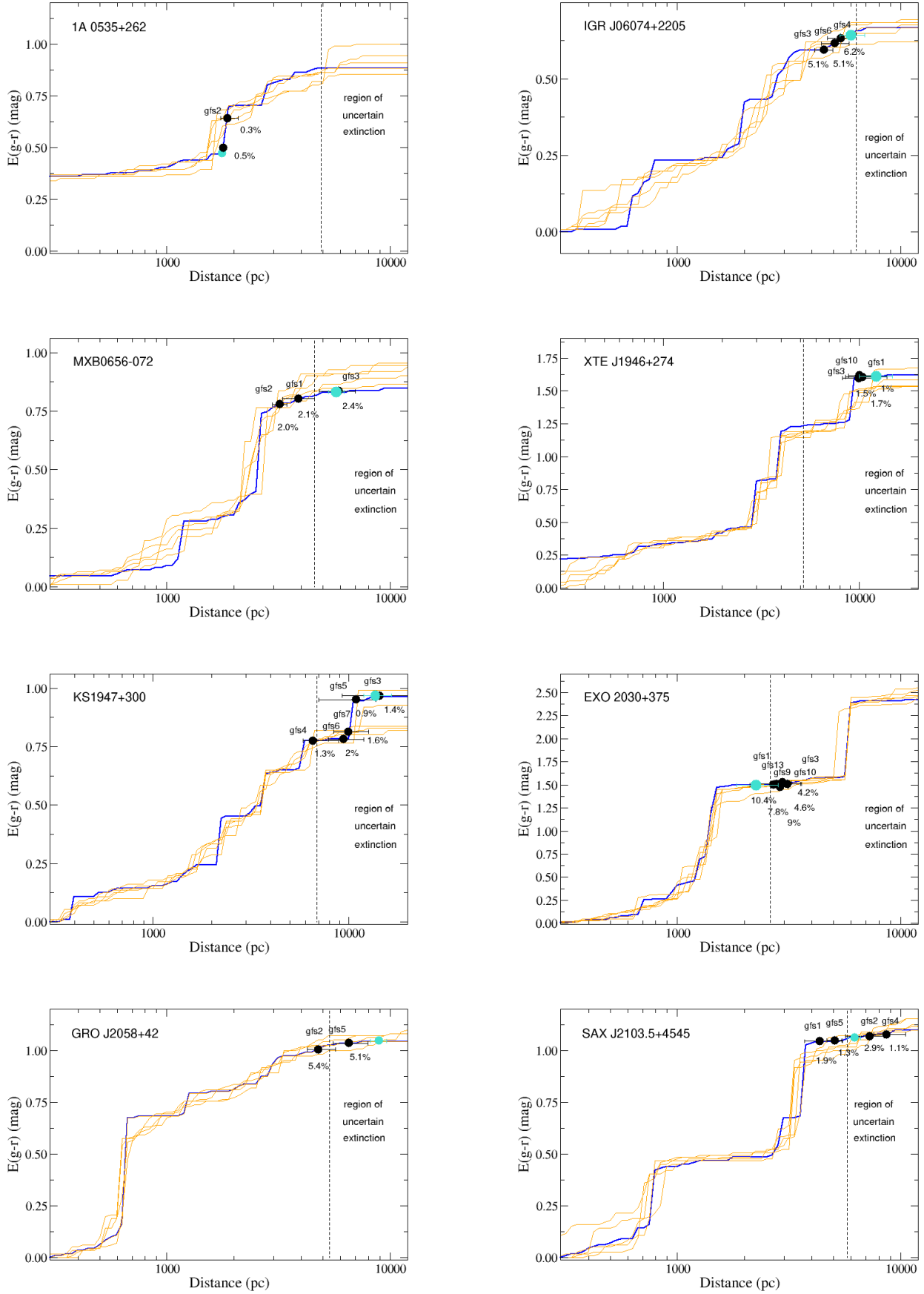


Fig. B.2: Continued.

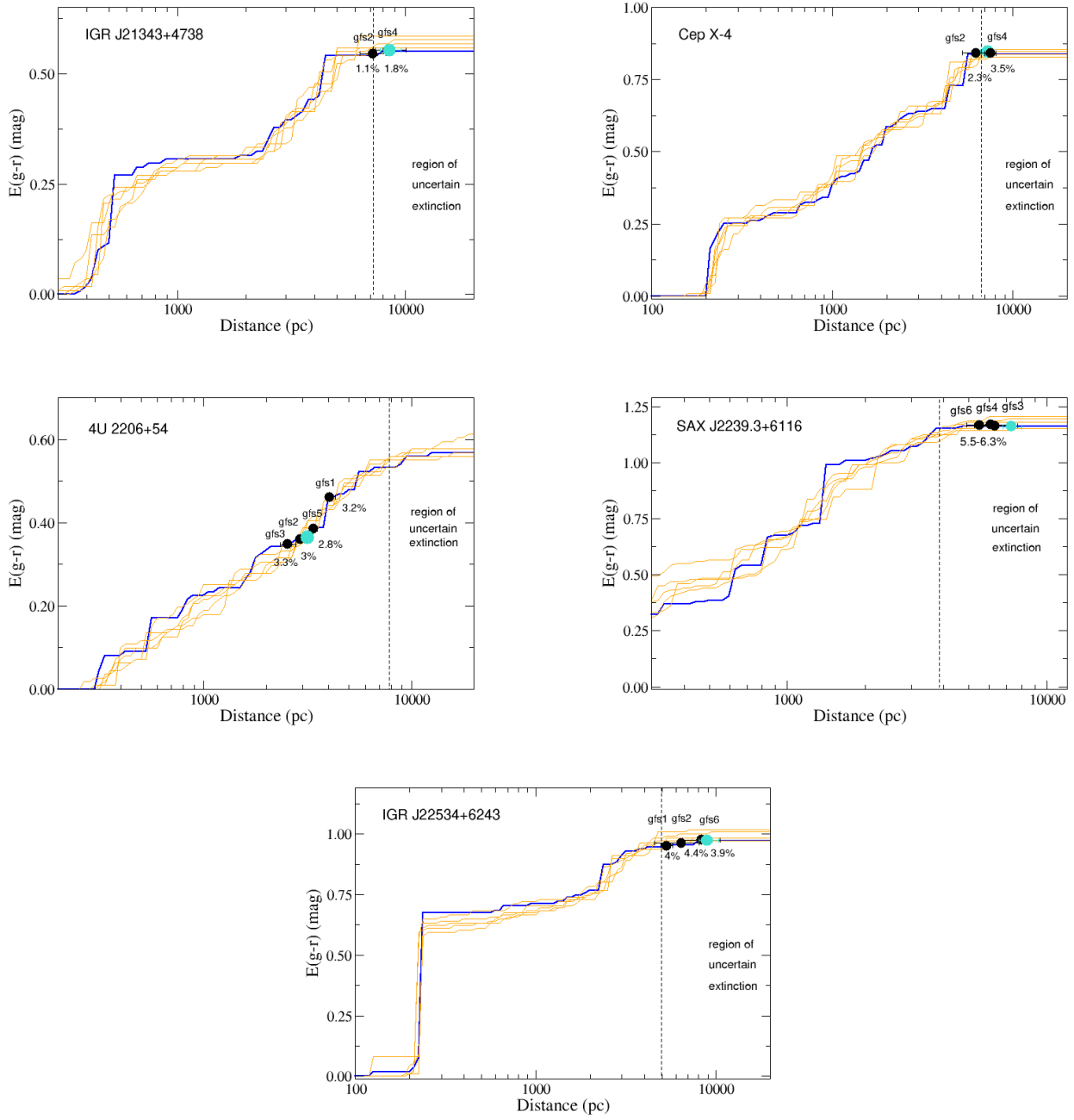


Fig. B.3: Continued.

Appendix C: Sky charts of field stars

Sky charts of the targets. The field of view is 12.5×12.5 arcmin. North is up, East is left. The target is marked in red, while the field stars are marked with blue circles.

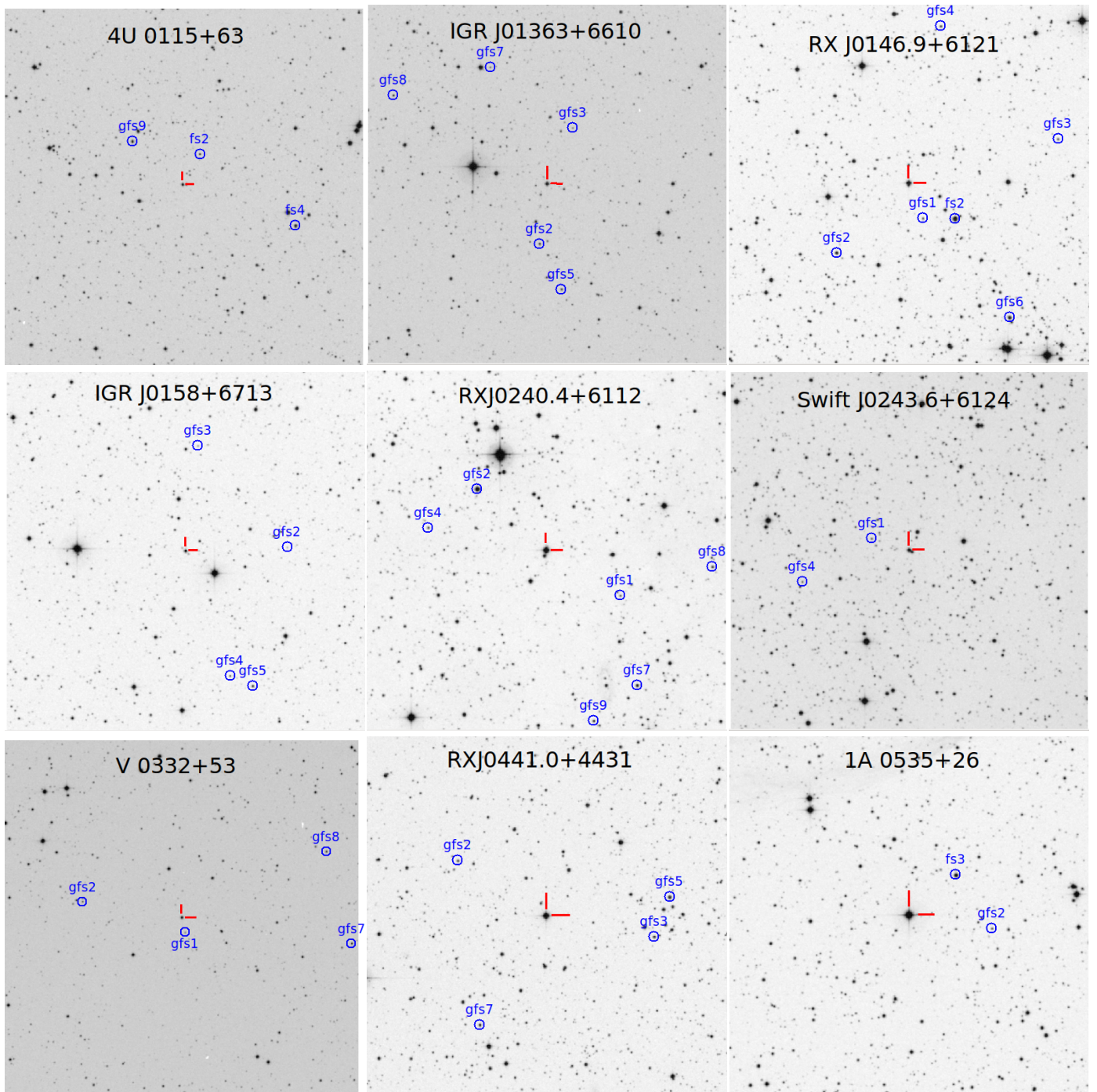


Fig. C.1: Sky charts with the identification of the target (red lines) and the field stars (blue circles).

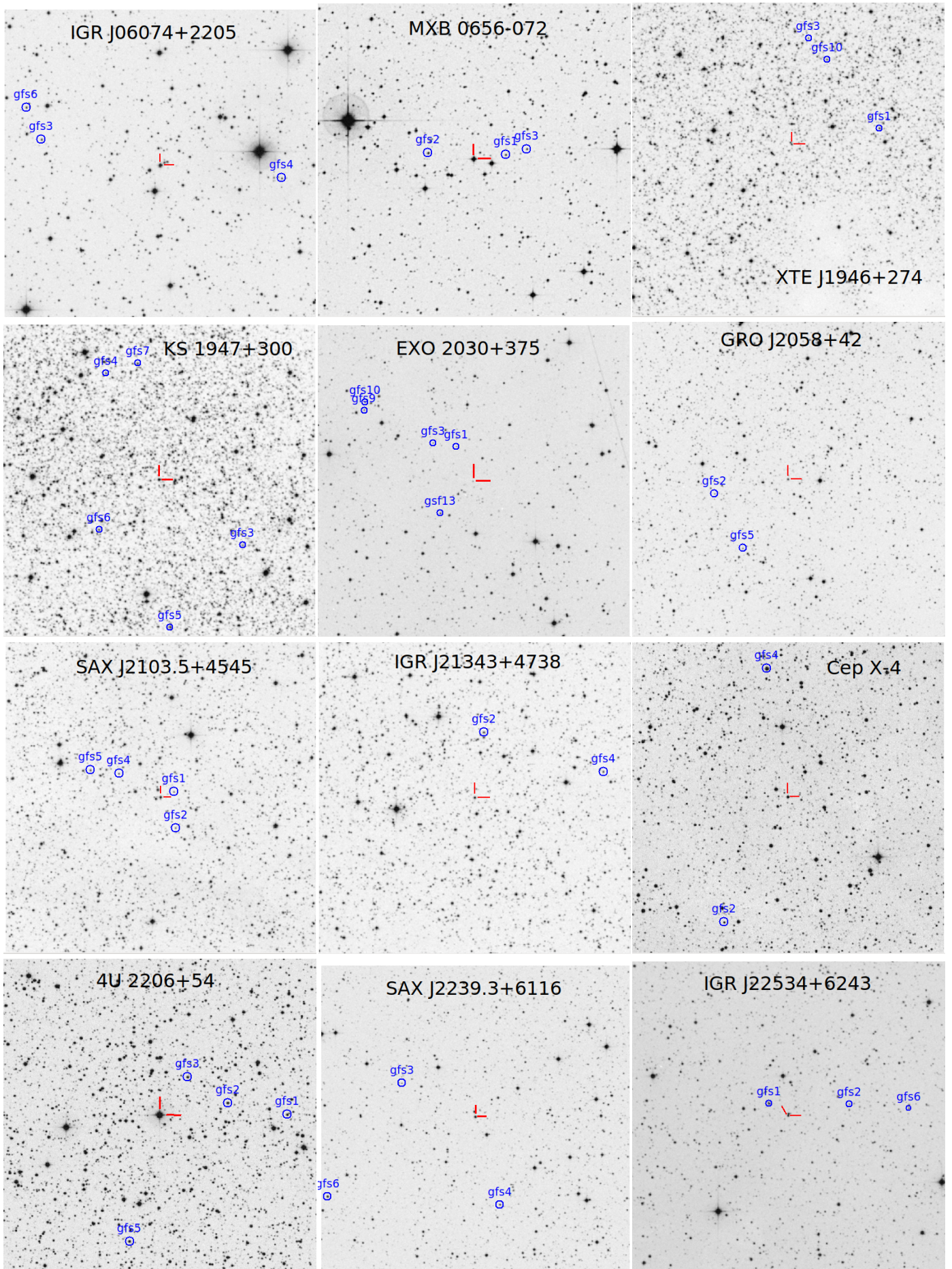


Fig. C.2: Continued.